Nanoscale

PAPER

View Article Online
View Journal | View Issue

Cite this: *Nanoscale*, 2023, **15**, 2882

Non-centrosymmetric Weyl semimetal state and strain effect in the twisted-brick phase transition metal monochalcogenides†

Jia-Fang Wu, [a] Sha-Sha Ke,*[a] Yong Guo,[b] Huai-Wu Zhang[a] and Hai-Feng Lü *[a,b]

Received 8th September 2022,
Accepted 6th January 2023

DOI: 10.1039/d2nr04946e

rsc.li/nanoscale

Weyl semimetals are a class of gapless electronic excitation topological quantum materials upon breaking time-reversal or inversion symmetry. Here, we demonstrate the existence of the Weyl semimetal state in the non-centrosymmetric twisted-brick phase MoTe theoretically. The topological properties and strain effects of MoTe have been systematically studied based on first-principles calculations and the Wannier-based tight-binding method. In the absence of spin–orbit coupling (SOC), MoTe exhibits gapless nodal loop states related to the mirror reflection symmetry. When the SOC is turned on, the two nodal loops split into 22 pairs of Weyl points (WPs) with opposite chirality. When the effect of uniaxial (ε_z) strain is taken into account, the Weyl semimetal phase of MoTe shows great robustness and striking tunable topological strength. In particular, the total number of WPs changes significantly under strain. MoTe under +4% and +8% uniaxial strains have only four pairs of WPs with a relatively large separation in momentum space. These results show that MoTe under weak strain is a promising partly ideal type I Weyl semimetal candidate, while the isolog structure WTe both opens a direct gap with and without SOC, showing a compensated semimetal state.

1. Introduction

The discovery of exotic topological states of matter is an active research field in condensed matter physics and materials science in the past decade. Topological materials such as topological insulators[1] and topological semimetals (TSMs) have potential applications in the spintronic field due to their novel physical properties. Three dimensional (3D) topological semimetal phases are the phases of matter with gapless electronic excitations that are protected by topology and symmetry,[2] in which the conduction and valence bands can cross each other either at discrete points (Dirac/Weyl semimetal)[3–7] or along a closed curve (nodal line/loop semimetal).[8–13] The gapless phases of 3D Weyl semimetal (WSM) are usually characterized by the 2D discontinuous Fermi surface boundary states (Fermi arcs) on the surfaces Brillouin zone (BZ).[2] The surface arc depends sensitively on the protected double degeneracy WPs near the Fermi level due to which the low-energy electron quasiparticles exhibit pseudospin, linear dispersions, and other features. Furthermore, the twofold degeneracy WPs suggests that WPs can only appear when the spin-doublet degeneracy of the bands is eliminated, which means that the time-reversal symmetry (TRS) or the inversion symmetry (IS) of the system should be broken. The chirality of WPs is also considered a topological charge analogous to the monopole or anti-monopole of Berry curvature. It can be quantized by the total Berry flux through a momentum space surface containing a single WP. Moreover, WSM is robust against any weak perturbation that preserves translational symmetry.[14] An exchange field or slight lattice distortion can only shift the positions of WPs.[4]

Recently, efficiently mass-searching topological materials by symmetry-based indicator and topological quantum chemical methods has attracted increasing attention, such as centrosymmetric nonmagnetic topological systems[15–17] and magnetic topological systems.[18] However, it cannot detect strongly correlated electronic systems whose low-energy quasiparticles are Dirac/Weyl fermions and non-centrosymmetric systems, whose band inversion is away from certain high-symmetry points. Non-centrosymmetric systems provide a promising arena to realize ideal Weyl semimetals with potential applications for low-power and high-speed electronics. Currently, there are several representative proposals for WSM systems that involve nonmagnetic materials by breaking the spatial IS.[19] The first proposal to realize non-centrosymmetric WSM in condensed-

[a]*School of Physics and State Key Laboratory of Electronic Thin Films and Integrated Devices, University of Electronic Science and Technology of China, Chengdu 610054, China. E-mail: keshasha@uestc.edu.cn, lvhf04@uestc.edu.cn*
[b]*Department of Physics and State Key Laboratory of Low-Dimensional Quantum Physics, Tsinghua University, Beijing 100084, China*

† Electronic supplementary information (ESI) available. See DOI: https://doi.org/10.1039/d2nr04946e

matter materials was suggested in ref. 20–22 for the TaAs family, where 12 pairs of WPs were derived from the nonzero mirror Chern numbers for two of the mirror-invariant planes. The T_d phase layered transition metal dichalcogenides (TMDs) discussed in ref. 23 and 24 is an example of a type-II Weyl semimetal, which in its incarnation demonstrates that the distribution of the WPs is found to be very sensitive to the lattice parameters. A magnetic non-centrosymmetric system PrAlGe was then proposed, which hosts the emergent topological properties of Weyl fermions by photoemission-based spectroscopy and magneto-transport.[25] The transition metal monochalcogenides (TMMs) system MoTe[26,27] and W_2SeS[28] were also proposed, in which 4 and 12 pairs of WPs due to band-crossing appear when the systems are with SOC, respectively. Recent experimental and theoretical studies on the non-centrosymmetric LaAlSi[29] and LaAlGe[30] unveiled the signatures of the type-I and type-II Weyl states. Undoubtedly, it is still an important task to search for WSM in non-centrosymmetric systems.

In this work, using density functional theory (DFT) calculations and the Wannier-based tight-binding method, we systematically studied the topological electronic properties and strain effects of the non-centrosymmetric twisted-brick phase TMMs, MoTe, and WTe. We mainly focused on the $Pmn2_1$-MoTe system, which presents a clear nodal loop state and WSM state near the Fermi level when SOC is absent and present, respectively. For completeness, we also carried out some calculations on the optimized WTe, such as energy bands with/without SOC, and the crossing points between the conduction band (CB) and the valence band (VB). The results show that WTe is a compensated semimetal with and without SOC. Moreover, we find that the topological properties in MoTe can be strikingly tuned by strain; thus, the WPs in MoTe are controllable.

The paper is organized as follows. In Section 2, we first described the crystal structural features and the stabilities of twisted-brick phase MoTe/WTe. Then, we provided the computational methods used. Next, we have considered the electronic properties and symmetries of MoTe and WTe. In Section 3, we investigated the effects of SOC on the topological properties of MoTe. At the end of this section, we discussed in detail the effects of uniaxial strain on the topological properties of MoTe, such as the total number of WPs, the average energy of WPs, and the length of the Fermi arc. Finally, we gave a summary in Section 4.

2. Calculation methods and crystal structure

To predict the "twisted-brick" phase MoTe/WTe hosting non-centrosymmetric topological WSM, we carried out the structural optimization and electronic structure calculations using density functional theory (DFT)[31] based on the projector-augmented wave method as implemented in the Vienna *Ab initio* Simulation Package (VASP) code.[32] The plane-wave kinetic energy cutoff is set at 550 eV. The exchange–correlation interaction was handled in the generalized gradient approximation parametrized by Perdew–Burke–Ernzerhof (PBE).[33] The Brillouin zones are sampled with 10 × 6 × 4 Monkhorst–Pack special *k*-point meshes for MoTe/WTe bulk. During structural relaxation, all lattices and atoms are fully relaxed until the Hellmann–Feynman forces are less than the convergence criteria of 0.001 eV $Å^{-1}$. The dynamic properties of MoTe and WTe were obtained by the DFPT method, which is realized in the Phonopy package.[34] The effect of with and without SOC interactions both are considered in the calculations of electronic structures. The novel topological properties of both MoTe and WTe are obtained by tight-binding (TB) models within maximum localized Wannier functions (MLWF),[35] as implemented in the software package Wannier90.[36] We chose Mo-*d*/W-*s*, *d*, and Te-*p* orbitals as the initial orbitals and projected them into localized Wannier orbitals to accurately reproduce the DFT-based bands near the Fermi energy. The identification of the positions of WPs and the nodal loops, the Berry curvature in the BZ, and the surface states are calculated by the WannierTools software package.[37] Also, all the crystal structures are plotted using the VESTA software.[38]

Both MoTe and WTe crystallize in the non-symmorphic space group $Pmn2_1$ (No. 31), which lacks inversion symmetry. The optimized lattice parameters of MoTe (WTe) are a = 3.279 Å, b = 5.794 Å, and c = 8.830 Å (a = 3.302 Å, b = 5.942 Å, and c = 8.721 Å). All the atoms are located at the 2*a Wyckoff* position of the $Pmn2_1$ space group; the reduced positions are shown in Table 1. The "twisted-brick" phase is named because the side view of the twisted-brick phase is like a wall stacked with twisted bricks, as illustrated in Fig. 1(a). The bulk BZ is shown in Fig. 1c, where high symmetry points are noted. The symmetries in the twisted-brick phase are generated by the following symmetry operations: (i) identity operation E, (ii) the mirror reflection M_{yz}, which is a reflection around the x = 0 plane,

$$M_{yz}: (x,y,z) \rightarrow (-x,y,z), \tag{1}$$

(iii) the glide reflection $\bar{M}_{xz}$, which consists of y = 0 plane reflection, followed by $a/2$ translation along the x axis and $c/2$ translation along the z axis,

$$\bar{M}_{xz}: (x,y,z) \rightarrow \left(x+\frac{a}{2}, -y, z+\frac{c}{2}\right), \tag{2}$$

and (iv) the twofold screw rotation $\bar{C}_{2z}$, which consists of π rotation around the $z = c/2$ line, followed by $a/2$ translation along the x axis.

$$\bar{C}_{2z}: (x,y,z) \rightarrow \left(-x+\frac{a}{2}, -y, z+\frac{c}{2}\right). \tag{3}$$

The symmetries are the same as that of T_d-WTe_2 and $MoTe_2$ (layered TMDs) identified as the typical type-II Weyl semimetals. The twisted-brick XTe (X = W, Mo) is a bulk structure without layers and with broken inversion symmetry. For the brick phase, a relatively simpler brick system, odd-atomic-layer Bi, is predicted to be a Dirac-line semimetal protected by symmetries in first-principles calculation.[39] In addition, in the optical lattice, the tilted brick-wall system exhibits a sequence of topological phase transitions.[40]

Table 1 Structural characterization of MoTe and WTe. The coordinates for *Wyckoff* position 2*a* of the $Pmn2_1$ (No. 31) space group. There are two distinct Wyckoff positions (indicated by bracketed numbers) for Mo/W and Te atoms

Atom	Wyck.	*x*	*y*	*z*	Atom	Wyck.	*x*	*y*	*z*
Mo (1)	2*a*	0.5	0.65	0.03	W (1)	2*a*	0	0.64	0.03
Mo (3)	2*a*	0.5	0.05	0.45	W (3)	2*a*	0	0.07	0.46
Te (1)	2*a*	0.5	0.33	0.80	Te (1)	2*a*	0	0.34	0.79
Te (3)	2*a*	0.5	0.18	0.15	Te (3)	2*a*	0	0.17	0.15

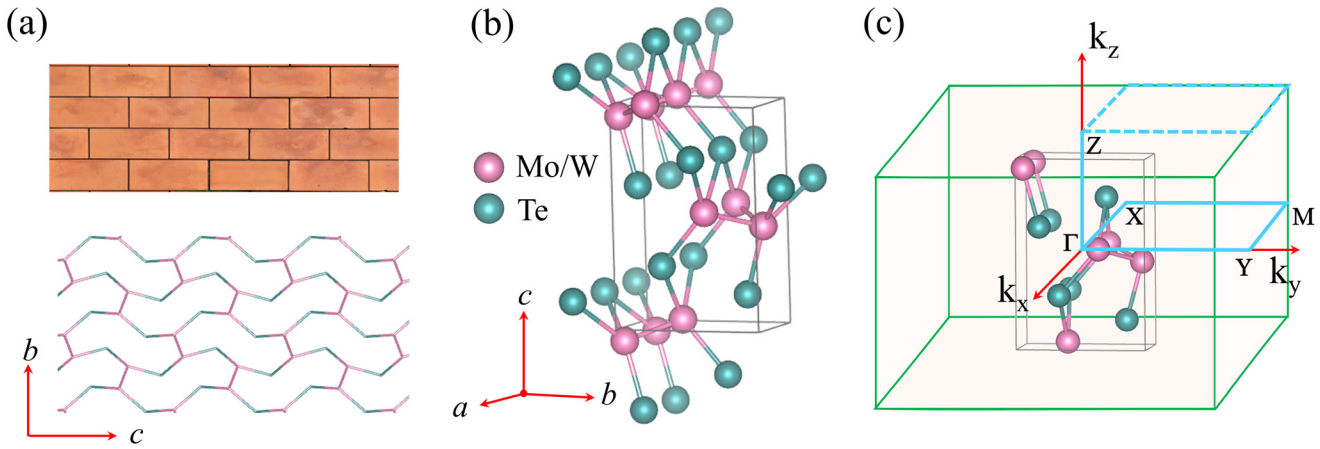

Fig. 1 Crystal structure and Brillouin zone (BZ). (a) Side view of the crystal structure of "twisted-brick" phase MoTe/WTe (the bottom panel) and the similar brick image (the upper panel). (b) Three-dimensional crystal structure of $Pmn2_1$-MoTe/WTe. Their space groups both are $Pmn2_1$ (No. 31). The pink and green balls denote Mo/W and Te atoms, respectively. (c) The bulk BZ with high symmetry points labeled.

The symmetry of the nonsymmorphic $Pmn2_1$ space group in the twisted-brick structure plays an important role in protecting the topological phases, which satisfies the requirement for generating WPs because it has broken inversion symmetry. It is important to note here that the mirror planes M_{yz} and $\bar{M}_{xz}$ contain the rotation *z* axis, which belongs to the C_{2v} point group. In addition, we confirmed the lattice dynamic stability and thermal stability of MoTe (see Fig. 2) and WTe (see ESI†) by calculating the phonon spectrum and a long-timescale AIMD simulation, respectively. We can see clearly that the phonon dispersion bands of MoTe have no negative frequencies, as shown in Fig. 2a, which indicates that the optimized twisted-brick structures are dynamically stable. The temperature and the total energy per unit cell of MoTe exhibit thermal fluctuations around the average up to 12 ps, as shown in Fig. 2 (b and c). In addition, we also presented the phonon, temperature, and total energy dispersions for MoTe under ε_z = +4% and +8% strain to identify their dynamic stability and thermal stability (see details in Section 4 of the ESI†).

3. Results and discussion

We first obtained the band structure of WTe without and with SOC by first-principles calculation and plotted it along the high-symmetry directions (see details in Section 1 of the ESI†). The results show that the band structure of WTe in the absence/presence of SOC both have a small direct gap with small trivial Fermi pockets along the high-symmetry line, exhibiting a compensated semimetal state. For MoTe, the results of first-principles calculation are summarized in Fig. 3. In the absence of SOC, the occupied band *N* and the band *N* + 1 cross each other twice along the Y–Γ line, which is indicated in the upper panel of Fig. 3a. The bands *N* + 2 and the *N* + 3 have no crossing points along the Y–Γ–X–M–Γ–Z line. There is a gap of 18.6 meV between the *N* + 2 and *N* + 3 bands along the Γ–X line at the suspected crossing points. By calculating the crossing points between the band *N* and the band *N* + 1 in the whole BZ, all the crossing points form two closed curves in the mirror M_{yz} plane, which can be confirmed by the 3D band dispersions, as illustrated in Fig. 4. Actually, the two crossing points along the Y–Γ line are a part of one closed curve in the mirror M_{yz} plane. The orbital-resolved analysis shows that the bands near the Fermi energy are mainly composed of Mo-5*d* orbitals, which have a large SOC effect. The nodal loop states of MoTe without SOC are double-checked by the HSE06 functional (see details in Section 2 of the ESI†). Identical conclusions were obtained in the HSE06 band structure. When SOC turns on, the degeneracy of the band structure is broken, and the electronic band structures are modified strongly. The bands open a gap and form discrete touching points on the non-symmetrical lines and planes, as plotted at the bottom of Fig. 3a. Due to the non-centrosymmetry and the SOC effect in MoTe, the energy bands are nondegenerate except for the

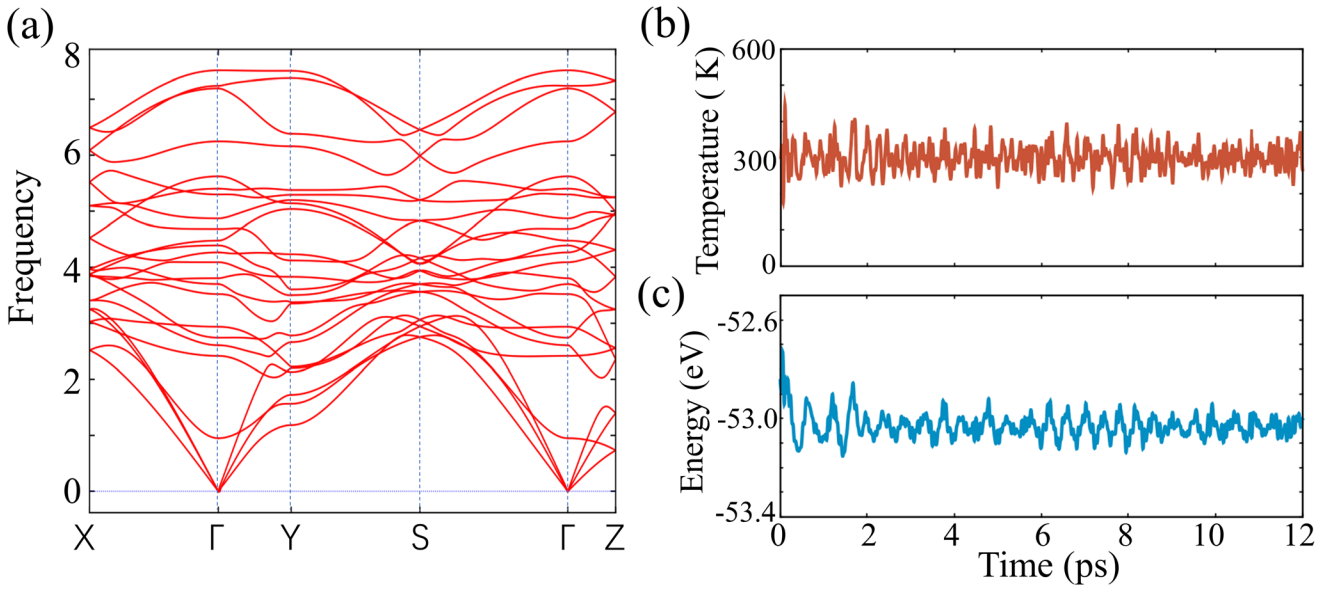

Fig. 2 The dynamic stability and thermal stability. (a) Phonon dispersion curve for the twisted-brick phase of MoTe. (b) The temperature and (c) total energy per unit cell as a function of simulation time in AIMD for MoTe.

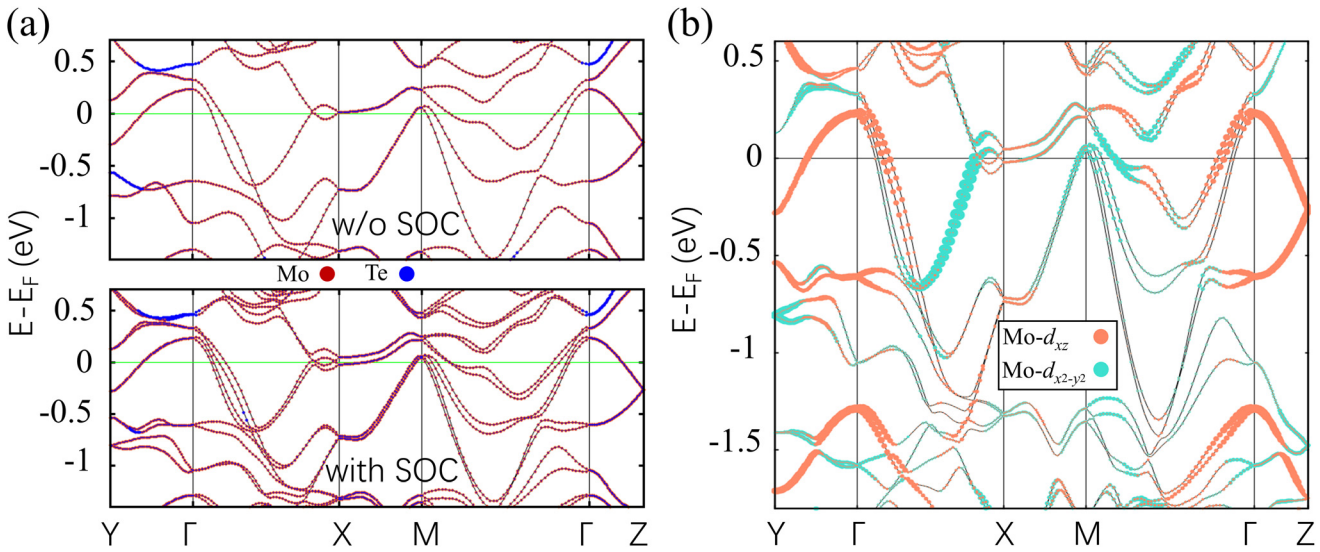

Fig. 3 Electronic structure of MoTe. (a) The band structure of MoTe without SOC (the upper panel) and with SOC (the bottom panel) near the Fermi level, respectively. The red and blue dots represent the contributions of Mo and Te atom orbitals, respectively. (b) Orbital-resolved band structures with SOC effect of MoTe. Different colored circles represent different orbital projections of Mo atoms, and the size of the circles represents the weight of the orbital projection.

time-reversal invariant points and lines of high symmetry. It should be pointed out that we determined the location of the possible touching points by searching the Wannier tight-binding bands throughout the BZ since band crossing points are away from certain high symmetry points and lines in the presence of SOC.

We further verify the contribution of the orbitals of the Mo atom to the bands near the Fermi level and identify the band inversion. From Fig. 3a, we conclude that the low-energy bands are mostly dominated by the contribution of the Mo-5*d* orbitals with a small Te-*p* orbitals admixture. We further performed an analysis of each orbital contribution of Mo 5d. From the results, we obtained that the crossing bands are mainly composed of the Mo-$d_{x^2-y^2}$ and Mo-d_{xz} orbitals. Particular emphasis is placed on the band inversion features near the Fermi level along the high symmetry line Γ–X, which can be indicated by orange and turquoise dots in Fig. 3b. Hence, there is a nontrivial band inversion between the Mo-$d_{x^2-y^2}$ and Mo-d_{xz} orbitals in the twisted-brick phase MoTe. Similar to many other typical WSMs, the topological phase in

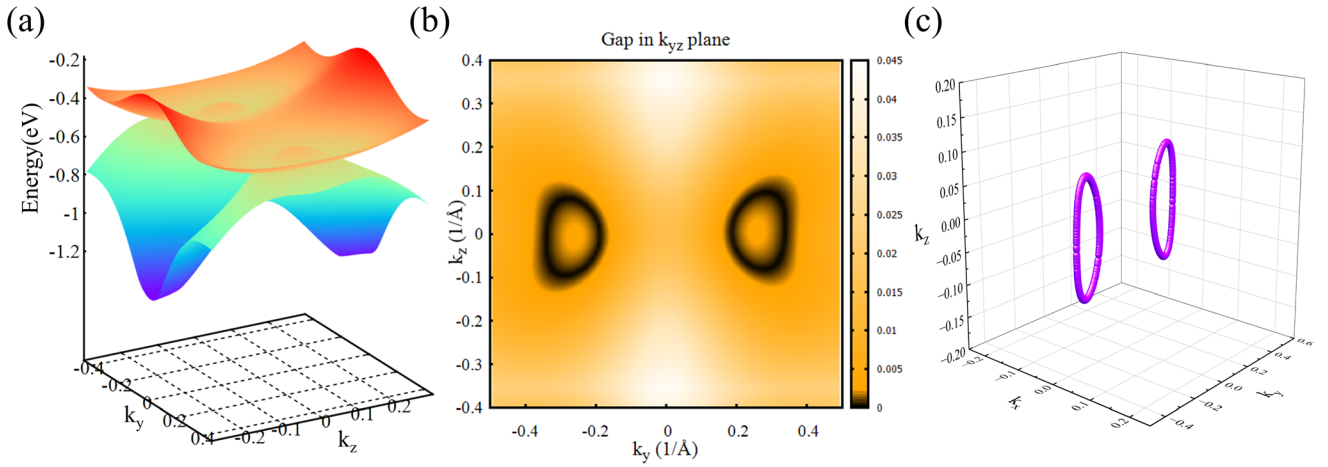

Fig. 4 The nodal ring states of MoTe without SOC. (a) The 3D band dispersions near the two nodal loops. (b) Energy gap ΔE (k_y, k_z) between the lowest conduction band and the top valence band at the k_x = 0 plane. (c) The positions of the nodal loops in the bulk Brillouin zone.

the MoTe system results from a band-inversion phenomenon in the absence of SOC (see details in Section 3 of the ESI†). At the same time, the two nontrivial nodal loops in the k_x = 0 mirror plane are symmetry-protected. When the SOC is considered, the nodal loops will split into pairs of WPs.

We first consider in detail the crossing points of MoTe at generic momenta (GM) points in the absence of SOC. The locations of all crossing points between the lowest CB and the top VB and the shape of the crossing points were obtained by the Wannier-based tight-binding method, as shown in Fig. 4. The results show that the crossing points are not independent, and it is residing on a nodal ring in the k_x = 0 plane (see Fig. 4c). The 3D energy bands around the nodal loop in plane k_{yz} is as shown in Fig. 4a, which reveals that the band crossing points in the plane form two closed nodal rings. It is also found that the energy of the crossing points is linear with slight energy variation along the loop. To clarify the feature of the nodal loops, the energy gap ΔE (k_x, k_z) between the two crossing bands is shown in Fig. 4b. It should be pointed out that the nodal ring of the current MoTe system is protected by the mirror reflection M_{yz} in the absence of SOC. We can see that the loops are located in the mirror-invariant k_x = 0 plane. The two crossing bands have opposite mirror eigenvalues, which means that the points will break away from the mirror symmetry protection as it moves away from the mirror plane. As a conclusion, in the absence of SOC, the twisted-brick phase MoTe is with topological nontrivial electronic states exhibiting two nodal loops around the Fermi level. Notably, the topological nodal loop states will change when SOC is considered.

Including SOC in calculation leads to a dramatic change of the band structure near the Fermi level of MoTe. Our calculation shows that the previous nodal loops in the k_{yz} plane are partially gapped in the presence of SOC, and the nodal loops split into 22 pairs of Weyl nodes with opposite chirality. To check the chirality of the WPs, we obtained the Berry curvature around them by the Wannier-based tight-binding method. Considering only the occupied bands as a joint band manifold, the discrete k mesh as the integration, and a series of close space points k_j as the closed curve, the formalism of the Berry phase ϕ and Berry curvature Ω are as follows

$$\phi = -\mathrm{Im}\ \ln \prod_j \det\langle u_{m,\boldsymbol{k}_j} | u_{n,\boldsymbol{k}_{j+1}} \rangle \tag{4}$$

$$\Omega_{\mathrm{mn},\alpha\beta} = -2\mathrm{Im}\langle \partial_\alpha u_{\mathrm{m},\boldsymbol{k}} | \partial_\beta u_{n,\boldsymbol{k}} \rangle \tag{5}$$

where $\alpha = k_x, k_y, k_z$. From Stokes theorem, if the closed curve encloses a Weyl point, the total integral of the Berry curvature of this closed torus must equal the total "monopole charge" carried by the Weyl point enclosed inside. In this way, we checked the chirality of each WPs using Wannier90. For example, Fig. 5a shows the Berry curvature of two pairs of WPs at $k_z = -0.2 \times 2\pi/c$ plane. As shown in Fig. 5b, it can be found that the selected WP acts as a source of the Berry curvature. Besides, the Wilson loop (Wannier charge center, WCC) is calculated for k_y = 0, 0.5 × $2\pi/c$ planes by WannierTools,[37] as shown in Fig. 5c. The WCC intersects an arbitrary reference line an odd number of times at the k_y = 0 plane, which gives a nontrivial Z_2 number (Z_2 = 1) and indicates topological nontriviality.

When SOC turns on, the two nodal loops split into 22 pairs of WPs. However, it is potentially more complicated with a higher number of WPs, and the minimum numbers of WPs in nonmagnetic Weyl semimetals are four. We thus propose an effective modulation way to optimize the topological properties of WSMs utilizing the strain effects, such as uniaxial strain along the z-axis (ε_z). We mainly focus on the changes in WPs within the −10% to +10% strain range, including the number of WPs (see Fig. 6a), the average energy of WPs and the k space distance (Δk) between a pair of WPs (see details in Section 5 of the ESI†). Our calculation shows that the number of WPs decreases rapidly under tensile strain. In particular, the

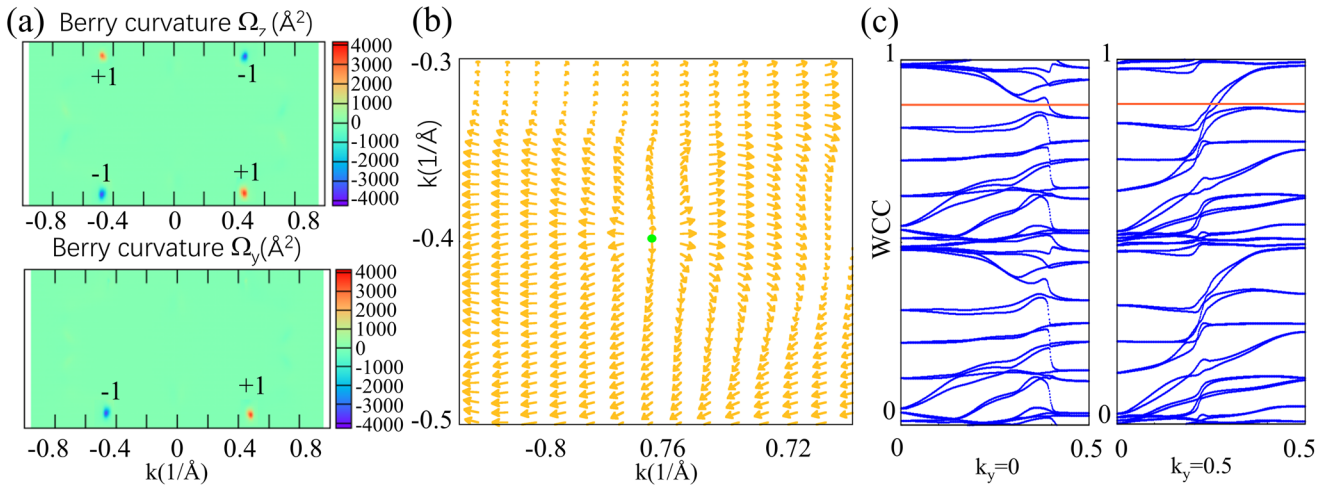

Fig. 5 Berry curvature and Wannier charge (WCC) center in MoTe with SOC. (a) The distribution of the Berry curvature for the k_y = 0 and k_z = 0 planes, where the red and blue dots denote the WPs with chirality of +1 and −1, respectively. (b) The 2D view of Berry curvature near the one selected Weyl point at k_z = 0.2108 plane. (c) The WCC at k_y = 0, 0.5 × 2π/c planes. The orange line is the arbitrary reference line.

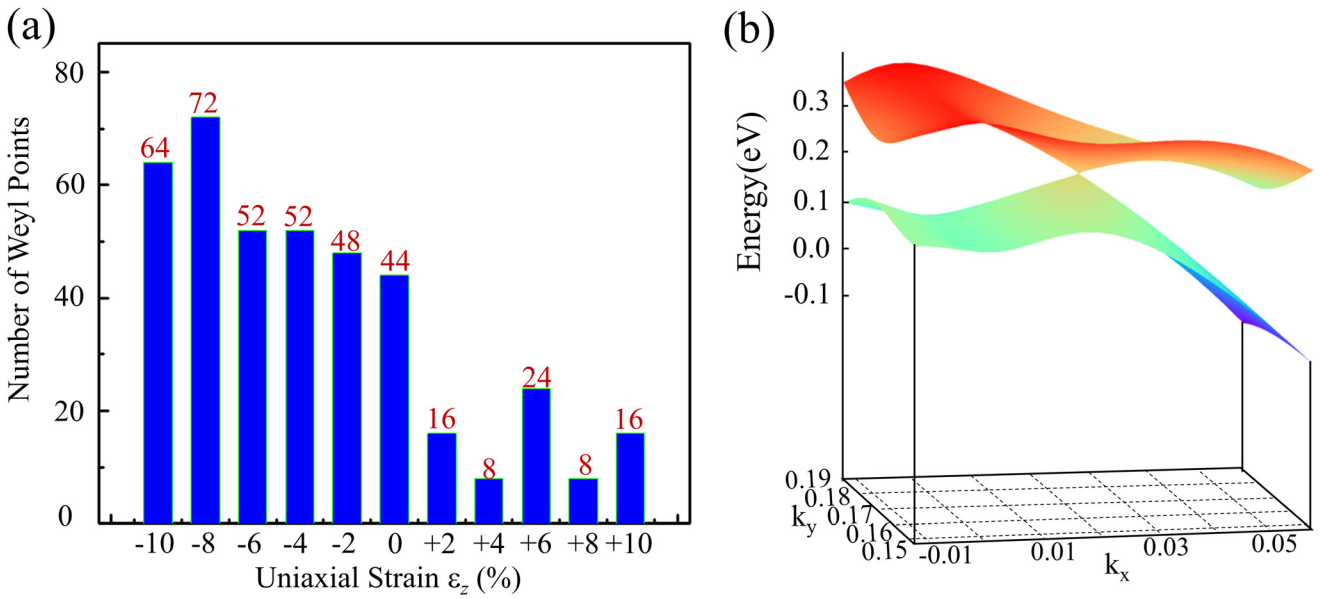

Fig. 6 The Weyl semimetal state under strain. (a) The variation of the number WPs under the uniaxial strain along the z direction for twisted-brick phase MoTe. (b) The 3D band dispersions around one Weyl node (0.033, 0.189, 0.124) under ε_z = +8% tensile strain.

Table 2 The locations, maximal separation (Δk), and chirality of two WPs (the quarter of the 8 Weyl nodes) for MoTe under ε_z = +4% and +8% strain, respectively. After considering time-reversal symmetry, two other WPs with the same chirality will be confirmed. Then, adding the M_{yz} mirror symmetry, the remaining four WPs with opposite chirality will also be obtained

Strain		Symmetry	Nodes	Coordinates $k_x(2\pi/a)$, $k_y(2\pi/b)$, $k_z(2\pi/c)$	Δk (Å^{-1})	Chirality
ε_z	+4%	M_{yz}+	WP1	(0.026, 0.170, 0.079)	0.36	−1
			WP2	(−0.001, 0.114, −0.0587)	0.26	−1
	+8%	M_{yz}+	WP1	(0.033, 0.189, 0.124)	0.45	−1
			WP2	(0.035, 0.188, −0.129)	0.46	−1

numbers are both reduced to eight under ε_z = +4% and +8% tensile strain. We pinpoint the WPs' locations of MoTe under ε_z = +4% and +8% tensile strain, as shown in Table 2. The coordinates and chirality of WPs under ε_z = +4% and +8% strain fully satisfy time-reversal symmetry and M_{yz} mirror symmetry, which support the result of symmetry protection. At the same time, through the two symmetries, we can obtain the eight WPs coordinates from the two irreducible nodes, as

given in Table 2. In addition, the total number of WPs always changes with a multiple of four (see Fig. 6a), which further highly reflects the symmetry protected by time-reversal symmetry and mirror symmetry (see ESI† for the discussion of strain effects in Section 5). Intriguingly, the length of the Fermi arc between the Weyl nodes changes larger under strain. Usually, an increasing Δk between WPs leads to the length of the Fermi arc and the topological strength than before. The Δk decreases first and then increases as the strain varies from compressive to tensile. For example, under ε_z = −6% strain, the k space separation Δk is found to be as large as 1.08 Å^{-1}. Another useful quantity is the average energy of WPs. It is interesting to note that in contrast to the evolution of Δk (Fig. 5S†), the energy of WPs shows a non-monotonous function of uniaxial strain. At +10% strain, the average energy of WPs is found to be as large as 0.24 eV. The energy is about −1.10 eV at 0% strain. Besides, we have checked the type of the Weyl cones under ε_z = +4% and +8% tensile strain. Our calculation clearly shows that constant energy surfaces are closed rather than open, which illustrates that WPs are type I Weyl cones, as seen in Fig. 6b.

There are several major characteristics for the WPs under ε_z = +4% and +8% tensile strain. Firstly, the number of WPs is both 8, which is one-third of the number in the typical non-centrosymmetric WSM TaAs.[22] Secondly, the energy dispersion around WPs formed a closed Fermi surface with a standard Weyl cone along the certain k direction, which pointed out the WPs observed in the MoTe material under strain are type I fermions. By the way, the Fermi arcs of these WPs under ε_z = +4%, and +8% reside entirely above the Fermi energy, which can be observed by the pump–probe angle-resolved photoemission spectroscopy (ARPES) technique.[41] Furthermore, the WPs have a relatively large separation in momentum space, which is one property of ideal WSMs. The maximal separations between two WPs under ε_z = +4% and +8% strain with opposite chirality are 0.36 Å^{-1} and 0.46 Å^{-1}, as shown in Table 2, respectively. It is observed that the separations are larger than some typical WSMs, such as TaAs ~0.074 Å^{-1},[22] $MoTe_2$ ~ 0.042 Å^{-1},[4] and W_2SeS ~ 0.24 Å^{-1}.[28]

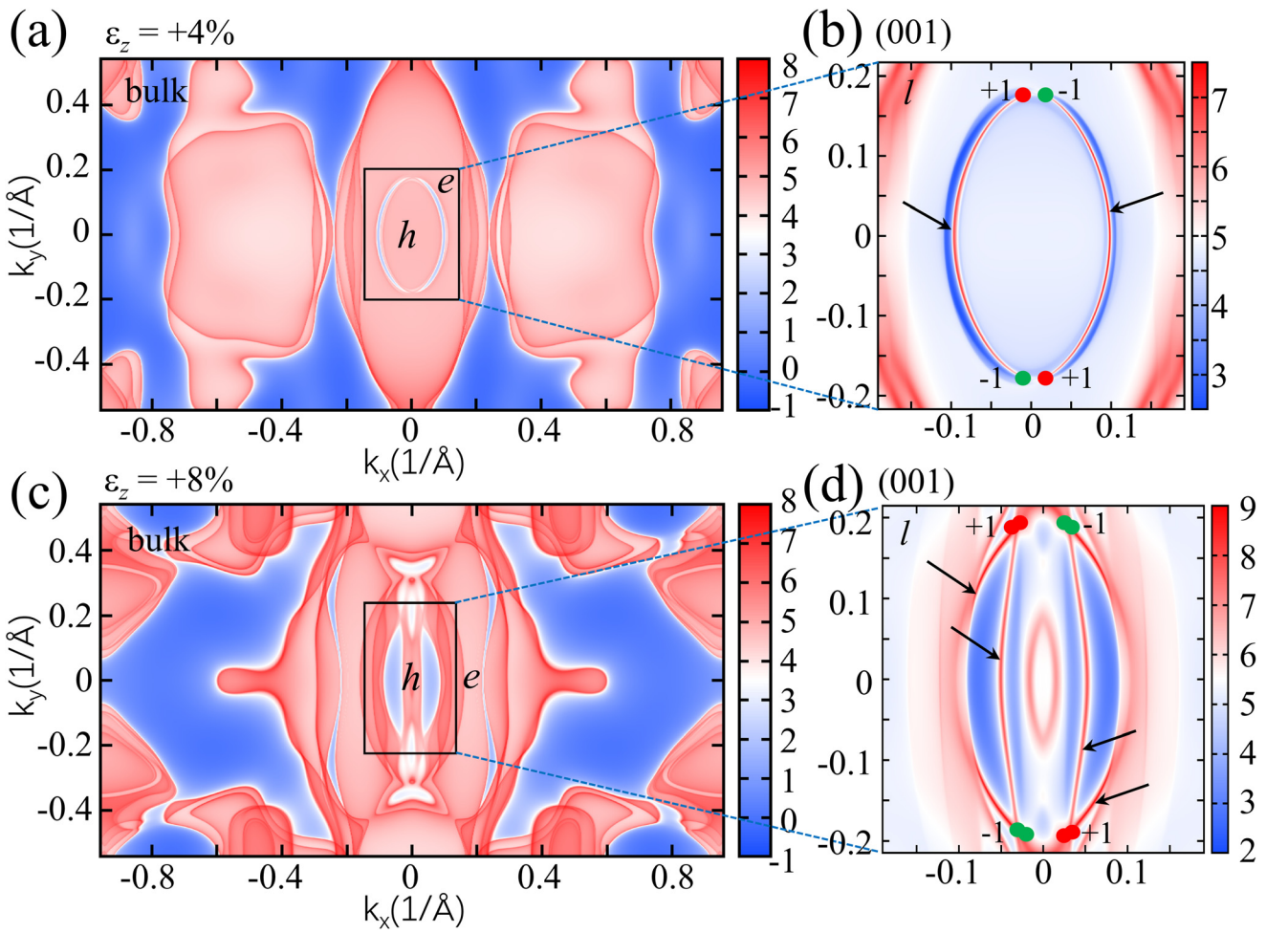

Fig. 7 Fermi arcs in the surface states. (a and c) Calculated $k_x - k_y$ bulk Fermi surface of MoTe under ε_z = +4% and +8% tensile strain, respectively. (b and d) Surface Fermi arcs in the (001) surface under ε_z = +4% and +8% tensile strain, respectively. The different colors represent the chirality of the Weyl points (red dot for positive and green dot for negative).

We have shown that applying small uniaxial strain along the z direction in twisted-brick MoTe can give rise to partly ideal type I WSM with only four pairs of Weyl nodes. Unique surface states with connected Fermi arcs can be found on the surface of a Weyl semimetal. We have computed the surface states for the (001) surface under ε_z = +4% and +8% tensile strain, as shown in Fig. 7. Both the bulk surface states exhibit a small hole-like pocket around the point Γ and a large electron-like pocket along the line Γ–X. It can be seen that the Weyl nodes are connected by the Fermi arc. In addition, the connectivity pattern of the Fermi arc under ε_z = +4% and +8% strain is shown in Fig. 7(b) and (d), respectively. Compared to other proposed WSM materials, this connectivity pattern guarantees the length of the Fermi arc, which greatly facilitates their detection in experiments. A very interesting point of the Fermi arc under ε_z = +4% strain is that the surface Fermi arcs form an approximately closed loop, as shown in Fig. 7b, which is similar to the Fermi arc shapes of TaAs.[22] The connectivity pattern of Fermi arcs is associated with exotic electron transport properties, which are expected to be verified in future experiments.

4. Conclusion

In conclusion, we theoretically report the topological properties and elucidated the strain effect on non-centrosymmetric twisted-brick compounds MoTe/WTe. Our calculations found that the MoTe compound appears a nontrivial nodal loop state in the mirror-invariant k_x = 0 plane in the absence of SOC. The nodal loop shows type-I band crossings. When SOC is considered, the nodal loops of MoTe are split into 22 pairs of WPs with opposite chirality. We found that the WSM phase of MoTe with SOC is robust against uniaxial strain along the z direction in the -10% –10% range. At the same time, the total number, average energy, and location of WPs can be controlled by the strain strength. Very interestingly, at ε_z = +4% and +8%, the total number of WPs reduced to four pairs. Therefore, the strain effect can tune the WPs to generate or annihilate new WPs. In addition, all the WPs located on the $k_x \neq 0$ planes are related by time-reversal symmetry and M_{yz} mirror symmetry. Also, all WPs are type I fermions. We also show that the strain can tune the length of the Fermi arc of MoTe, reaching approximately of the order of magnitude 0.1 $Å^{-1}$, which can be observed by pump–probe ARPES experiments. Also, the average energy of WPs shows a non-monotonous function of uniaxial strain. Remarkably, we revealed that WTe shows a compensated semimetal state with and without SOC. This study unveils the topological electronic properties of MoTe/WTe and further extends the promising material candidate of the ideal type I WSM with centrosymmetric breaking.

Conflicts of interest

There are no conflicts to declare.

Acknowledgements

This work was supported by the Natural Science Foundation of China under Grants No. 12074209 and No. 12274063, the Fundamental Research Funds for the Central Universities (No. ZYGX2019J100), and the Open Project of State Key Laboratory of Low-Dimensional Quantum Physics (Grant No. KF202008). The numerical calculations in this paper have been done on Hefei advanced computing center.

References

1 Z. Guo, X. Hao, J. Dong, H. Li, Y. Gong, D. Yang, J. Liao, S. Chu, Y. Li, X. Li and D. Chen, *Nanoscale*, 2020, **12**, 22710–22717.
2 N. P. Armitage, E. J. Mele and A. Vishwanath, *Rev. Mod. Phys.*, 2018, **90**, 015001.
3 T. O. Wehling, A. M. Black-Schaffer and A. V. Balatsky, *Adv. Phys.*, 2014, **63**, 1–76.
4 Z. Wang, D. Gresch, A. A. Soluyanov, W. Xie, S. Kushwaha, X. Dai, M. Troyer, R. J. Cava and B. A. Bernevig, *Phys. Rev. Lett.*, 2016, **123**(18), 186401.
5 A. L. D. F. Liu, E. K. Liu, Q. N. Xu, Y. W. Li, C. Chen, D. Pei, W. J. Shi, S. K. Mo, P. Dudin, T. Kim, C. Cacho, G. Li, Y. Sun, L. X. Yang, Z. K. Liu, S. S. P. Parkin, C. Felser and Y. L. Chen, *Science*, 2019, **365**(6459), 1282–1285.
6 N. Morali, R. Batabyal, P. K. Nag, E. Liu, Q. Xu, Y. Sun, B. Yan, C. Felser, N. Avraham and H. Beidenkopf, *Science*, 2019, **365**(6459), 1286–1291.
7 X. Wang, D. Pan, Q. Zeng, X. Chen, H. Wang, D. Zhao, Z. Xu, Q. Yang, J. Deng, T. Zhai, G. Wu, E. Liu and J. Zhao, *Nanoscale*, 2021, **13**, 2601–2608.
8 Y. Kim, B. J. Wieder, C. L. Kane and A. M. Rappe, *Phys. Rev. Lett.*, 2015, **115**, 036806.
9 T. Bzdusek, Q. Wu, A. Ruegg, M. Sigrist and A. A. Soluyanov, *Nature*, 2016, **538**, 75–78.
10 B. Feng, B. Fu, S. Kasamatsu, S. Ito, P. Cheng, C. C. Liu, Y. Feng, S. Wu, S. K. Mahatha, P. Sheverdyaeva, P. Moras, M. Arita, O. Sugino, T. C. Chiang, K. Shimada, K. Miyamoto, T. Okuda, K. Wu, L. Chen, Y. Yao and I. Matsuda, *Nat. Commun.*, 2017, **8**, 1007.
11 B. Feng, R. W. Zhang, Y. Feng, B. Fu, S. Wu, K. Miyamoto, S. He, L. Chen, K. Wu, K. Shimada, T. Okuda and Y. Yao, *Phys. Rev. Lett.*, 2019, **123**, 116401.
12 W. Meng, W. Liu, X. Zhang, Y. Liu, X. Dai and G. Liu, *Nanoscale*, 2021, **13**, 3194–3200.
13 P. Yan, T. Ouyang, C. He, J. Li, C. Zhang, C. Tang and J. Zhong, *Nanoscale*, 2021, **13**, 3564–3571.
14 Y. Sun, S.-C. Wu and B. Yan, *Phys. Rev. B: Condens. Matter Mater. Phys.*, 2015, **92**, 115428.
15 T. Zhang, Y. Jiang, Z. Song, H. Huang, Y. He, Z. Fang, H. Weng and C. Fang, *Nature*, 2019, **566**, 475–479.
16 M. G. Vergniory, L. Elcoro, C. Felser, N. Regnault, B. A. Bernevig and Z. Wang, *Nature*, 2019, **566**, 480–485.

17 F. Tang, H. C. Po, A. Vishwanath and X. Wan, *Nature*, 2019, **566**, 486–489.
18 Y. Xu, L. Elcoro, Z. D. Song, B. J. Wieder, M. G. Vergniory, N. Regnault, Y. Chen, C. Felser and B. A. Bernevig, *Nature*, 2020, **586**, 702–707.
19 H. Gao, J. Strockoz, M. Frakulla, J. W. F. Venderbos and H. Weng, *Phys. Rev. B*, 2021, **103**, 205151.
20 L. X. Yang, Z. K. Liu, Y. Sun, H. Peng, H. F. Yang, T. Zhang, B. Zhou, Y. Zhang, Y. F. Guo, M. Rahn, D. Prabhakaran, Z. Hussain, S. K. Mo, C. Felser, B. Yan and Y. L. Chen, *Nat. Phys.*, 2015, **11**, 728–732.
21 B. Q. Lv, H. M. Weng, B. B. Fu, X. P. Wang, H. Miao, J. Ma, P. Richard, X. C. Huang, L. X. Zhao, G. F. Chen, Z. Fang, X. Dai, T. Qian and H. Ding, *Phys. Rev. X*, 2015, **5**, 031013.
22 H. Weng, C. Fang, Z. Fang, B. A. Bernevig and X. Dai, *Phys. Rev. X*, 2015, **5**, 011029.
23 J. Jiang, Z. K. Liu, Y. Sun, H. F. Yang, C. R. Rajamathi, Y. P. Qi, L. X. Yang, C. Chen, H. Peng, C. C. Hwang, S. Z. Sun, S. K. Mo, I. Vobornik, J. Fujii, S. S. Parkin, C. Felser, B. H. Yan and Y. L. Chen, *Nat. Commun.*, 2017, **8**, 13973.
24 P. Hein, S. Jauernik, H. Erk, L. Yang, Y. Qi, Y. Sun, C. Felser and M. Bauer, *Nat. Commun.*, 2020, **11**, 2613.
25 D. S. Sanchez, G. Chang, I. Belopolski, H. Lu, J. X. Yin, N. Alidoust, X. Xu, T. A. Cochran, X. Zhang, Y. Bian, S. S. Zhang, Y. Y. Liu, J. Ma, G. Bian, H. Lin, S. Y. Xu, S. Jia and M. Z. Hasan, *Nat. Commun.*, 2020, **11**, 3356.
26 J. F. Wu, S. S. Ke, Y. Guo, H. W. Zhang and H. F. Lu, *Phys. Chem. Chem. Phys.*, 2021, **23**, 23196–23202.
27 L. Meng, J. Wu, Y. Li and J. Zhong, *J. Mater. Chem. C*, 2019, **7**, 12151–12159.
28 L. Meng, J. Wu, Y. Li, L. Zhao and J. Zhong, *Phys. Rev. B*, 2019, **100**, 155151.
29 H. Su, X. Shi, J. Yuan, Y. Wan, E. Cheng, C. Xi, L. Pi, X. Wang, Z. Zou, N. Yu, W. Zhao, S. Li and Y. Guo, *Phys. Rev. B*, 2021, **103**, 165128.
30 M. Corasaniti, R. Yang, Z. Hu, M. Abeykoon, C. Petrovic and L. Degiorgi, *Phys. Rev. B*, 2021, **104**, L121112.
31 P. J. Perdew, *Phys. Rev. B: Condens. Matter Mater. Phys.*, 1986, **33**(12), 8822.
32 G. Kresse and J. Furthmüller, *Comput. Mater. Sci.*, 1996, **6**, 15–50.
33 J. P. Perdew, K. Burke and M. Ernzerhof, *Phys. Rev. Lett.*, 1996, **77**(18), 3865.
34 A. Togo and I. Tanaka, *Scr. Mater.*, 2015, **108**, 1–5.
35 N. Marzari, A. A. Mostofi, J. R. Yates, I. Souza and D. Vanderbilt, *Rev. Mod. Phys.*, 2012, **84**, 1419–1475.
36 A. A. Mostofi, J. R. Yates, Y.-S. Lee, I. Souza, D. Vanderbilt and N. Marzari, *Comput. Phys. Commun.*, 2008, **178**, 685–699.
37 Q. Wu, S. Zhang, H.-F. Song, M. Troyer and A. A. Soluyanov, *Comput. Phys. Commun.*, 2018, **224**, 405–416.
38 K. Momma and F. Izumi, *J. Appl. Crystallogr.*, 2008, **41**, 653–658.
39 D. Guo, P. Guo, S. Tan, M. Feng, L. Cao, Z.-X. Liu, K. Liu, Z.-Y. Lu and W. Ji, *Sci. Bull.*, 2022, **67**, 1954–1957.
40 A. R. Kolovsky, *Phys. Rev. A*, 2018, **98**, 013603.
41 I. Belopolski, P. Yu, D. S. Sanchez, Y. Ishida, T. R. Chang, S. S. Zhang, S. Y. Xu, H. Zheng, G. Chang, G. Bian, H. T. Jeng, T. Kondo, H. Lin, Z. Liu, S. Shin and M. Z. Hasan, *Nat. Commun.*, 2017, **8**, 942.

